Perspective in Oncology Management and Research

https://pomr.cultechpub.com/pomr

Cultech Publishing

Review

Transcriptomic Analysis Reveals Mitochondrial and Cytoskeletal Rewiring in Anlotinib-Treated Non-Small Cell Lung Cancer Cells

Awais Ali[1,*], Syed Yasir Ali[2]

[1]Department of Biochemistry, Abdul Wali khan university, Mardan, Pakistan

[2]Department of Pathology, Abdul Wali Khan University, Mardan, Pakistan

[*]Corresponding author: Awais Ali, awaisalibio@gmail.com

Abstract

The dense extracellular matrix (ECM) and elevated mechanical stress within solid tumors significantly hinder antitumor drug penetration and therapeutic efficacy. Anlotinib, a multi-target tyrosine kinase inhibitor, has emerged as a promising agent capable of improving intratumoral drug distribution; however, the mitochondrial mechanisms underlying its stromal-modulating effects remain insufficiently characterized. RNA-sequencing data from Anlotinib-treated and control A549 non-small cell lung cancer (NSCLC) cells were retrieved from the GEO database (GSE237818). Differentially expressed genes (DEGs) were identified using DESeq2. A comprehensive mitochondrial and oxidative phosphorylation gene panel was curated from MitoCarta3.0, MitoPathways, Molecular Signatures Database (MSigDB), and Reactome. Mitochondrial-related differentially expressed genes (MG-DEGs) were identified by intersecting DEGs with mitochondrial gene sets. Protein-protein interaction (PPI) networks were constructed using STRING, hub genes were identified using CytoHubba, and functional enrichment analyses were performed using Gene Ontology (GO) and pathway databases. Anlotinib treatment induced widespread transcriptional remodeling in NSCLC cells, with robust differential expression across multiple metabolic and structural pathways. Intersection analysis identified 191 mitochondrial-related DEGs, indicating selective modulation of mitochondrial function. PPI analysis revealed tightly interconnected mitochondrial networks, with hub genes enriched in oxidative phosphorylation, electron transport chain activity, and mitochondrial ATP synthesis. Functional enrichment further demonstrated significant associations with cytoskeletal organization and RhoA/Rho-associated protein kinase (ROCK) signaling pathways, suggesting a mechanistic link between mitochondrial metabolism, ECM remodeling, and tumor mechanical properties. Collectively, this integrative transcriptomic analysis identifies mitochondrial bioenergetic reprogramming as a prominent feature of Anlotinib-treated NSCLC cells and suggests a potential association between mitochondrial metabolism and tumor mechanical regulatory pathways. These findings are hypothesis-generating and provide a computational framework for future experimental studies investigating the mitochondrial-ECM interplay in tumor drug response.

Keywords

Anlotinib, Non-small cell lung cancer, Mitochondrial metabolism, Oxidative phosphorylation, Extracellular matrix remodeling, RhoA/ROCK signaling, Bioinformatics, RNA-sequencing, Bioinformatics analysis, Tumor drug targeting

Article History

Received: 01 January 2026
Revised: 16 February 2026
Accepted: 05 March 2026
Available Online: 10 March 2026

1. Introduction

Non-small cell lung cancer (NSCLC) remains the leading cause of cancer-related mortality worldwide, largely due to therapeutic resistance and limited drug penetration within solid tumors [1-4]. Although targeted therapies and immune checkpoint inhibitors have significantly improved clinical outcomes, their efficacy is frequently compromised by the dense extracellular matrix (ECM), elevated interstitial fluid pressure, and increased solid stress that characterize the tumor microenvironment. These physical barriers restrict intratumoral drug distribution, reduce local drug concentration, and ultimately contribute to treatment failure [5-7].

Recent evidence suggests that remodeling of the tumor ECM and reduction of mechanical stress can substantially improve drug delivery and therapeutic responsiveness. The RhoA/Rho-associated protein kinase (ROCK) signaling pathway plays a central role in regulating cytoskeletal tension, actin stress fiber formation, and cellular contractility, thereby influencing ECM stiffness and tumor solid pressure. Aberrant activation of RhoA/ROCK signaling has been implicated in tumor progression, metastasis, and resistance to chemotherapy and immunotherapy in NSCLC. Consequently, pharmacological inhibition of this pathway represents a promising strategy to normalize tumor biomechanics and enhance therapeutic efficacy. Anlotinib is a novel, orally administered multi-target tyrosine kinase inhibitor that blocks angiogenic and proliferative signaling pathways, including VEGFR, FGFR, PDGFR, and c-Kit. Beyond its established anti-angiogenic effects, emerging studies demonstrate that Anlotinib can modulate the physical properties of the tumor stroma by reducing ECM deposition [8], loosening tumor tissue architecture, and lowering interstitial and solid pressures. These biomechanical changes have been shown to prolong intratumoral drug retention and improve the distribution of chemotherapeutic agents, targeted therapies, and immune checkpoint inhibitors. However, the molecular mechanisms linking Anlotinib treatment to ECM remodeling and cytoskeletal regulation remain incompletely understood.

Mitochondria are central regulators of cellular energy metabolism, redox homeostasis, and mechanotransduction. Alterations in mitochondrial oxidative phosphorylation and ATP production can profoundly influence cytoskeletal dynamics, actomyosin contractility [9,10], and ECM interactions. Increasing evidence indicates that mitochondrial metabolism is tightly coupled to RhoA/ROCK signaling and cytoskeletal organization, thereby linking bioenergetic state to cellular mechanical properties [9,11]. In cancer cells, dysregulated mitochondrial function not only supports metabolic reprogramming but also contributes to tumor stiffness, invasive behavior, and therapeutic resistance. Despite this growing recognition, the role of mitochondrial gene regulation in mediating Anlotinib-induced stromal and mechanical remodeling in NSCLC has not been systematically explored.

High-throughput transcriptomic profiling provides a powerful approach to dissect drug-induced molecular networks and identify key regulatory pathways. Publicly available RNA-sequencing datasets offer an opportunity to interrogate the transcriptional effects of Anlotinib at a systems level. In particular, the GEO dataset GSE237818 profiles gene expression changes in A549 NSCLC cells following Anlotinib treatment, enabling integrative bioinformatics analysis of metabolic, structural, and signaling pathways associated with improved tumor drug targeting [12].

In the present study, we performed a comprehensive transcriptomic and network-based analysis of Anlotinib-treated NSCLC cells to elucidate mitochondrial mechanisms underlying ECM remodeling and RhoA/ROCK pathway modulation. Differentially expressed genes (DEGs) were identified and integrated with curated mitochondrial and oxidative phosphorylation gene sets to define mitochondrial-related differentially expressed genes (MG-DEGs). Protein-protein interaction (PPI) network construction, hub gene identification, and functional enrichment analyses were subsequently applied to uncover key mitochondrial regulatory nodes and pathways. Through this integrative framework, we provide novel insight into how Anlotinib-driven mitochondrial reprogramming may contribute to reduced tumor stiffness and enhanced intratumoral drug delivery, offering a mechanistic basis for rational combination therapy strategies in NSCLC.

2. Methodology

2.1 Transcriptomic Data Retrieval and Sample Information

RNA-sequencing data were retrieved from the National Center for Biotechnology Information (NCBI) Gene Expression Omnibus (GEO; https://www.ncbi.nlm.nih.gov/geo/) under accession number GSE237818 [13,14].This dataset was generated to investigate the molecular effects of Anlotinib treatment in human NSCLC. The experimental model consisted of the A549 lung adenocarcinoma cell line treated with Anlotinib or vehicle control (dimethyl sulfoxide, DMSO) for 48 hours. Gene expression profiling was performed using high-throughput RNA sequencing on the Illumina NovaSeq 6000 platform (GPL24676) [15,16]. A total of six samples were included in the analysis, comprising three Anlotinib-treated samples and three DMSO-treated control samples. Raw gene-level read count matrices were downloaded directly from the GEO repository and used as input for downstream bioinformatics analyses. Sample annotations were manually curated to ensure accurate grouping and experimental condition assignment.

2.2 Differential Gene Expression Analysis

Prior to differential expression analysis, only protein-coding genes were retained from the raw count matrix to improve biological interpretability and eliminate potential confounding effects from non-coding transcripts. Genes with very low expression across all samples were also filtered out according to DESeq2's default independent filtering procedure.Differential gene expression analysis was performed using the DESeq2 package (version 1.40.2) in R software (version 4.3.1), available through Bioconductor (https://bioconductor.org/packages/DESeq2/) [17,18]. Raw read counts were normalized using DESeq2's median-of-ratios method to correct for variations in sequencing depth and RNA composition among samples. Gene-wise dispersion estimates were calculated and fitted to a parametric dispersion trend to accurately model biological variability. Statistical testing was conducted using a negative binomial generalized linear model. Resulting p-values were adjusted for multiple comparisons using the Benjamini-Hochberg false discovery rate (FDR) correction method. Genes satisfying the criteria of $|\log2 \text{ fold change } (\log2FC)| \geq 1$ and adjusted p-value < 0.05 were considered significantly DEGs. This threshold was applied consistently across all downstream analyses, including functional enrichment and PPI network construction. To evaluate data quality and statistical robustness, several diagnostic plots were generated using ggplot2 (version 3.4.4), including volcano plots, MA plots, dispersion plots, and normalized count boxplots [19-21]. These visualizations were used to assess replicate consistency, distribution patterns, and model performance.

2.3 Retrieval of Mitochondrial and Oxidative Phosphorylation-Related Gene Sets

To comprehensively characterize mitochondrial involvement in Anlotinib-mediated transcriptional changes, mitochondrial and oxidative phosphorylation-related gene sets were curated from multiple high-confidence databases. The primary mitochondrial gene reference was MitoCarta3.0 (https://www.broadinstitute.org/mitocarta) [9], a rigorously curated inventory of 1,136 human mitochondrial proteins provided by the Broad Institute. The human annotation file (Human.MitoCarta3.0) was downloaded, and genes were extracted based on experimentally validated mitochondrial localization and functional annotation [22]. To specifically enrich oxidative phosphorylation-associated processes, additional genes were retrieved from the MitoPathways framework, which categorizes mitochondrial genes involved in electron transport chain complexes I-V, mitochondrial ATP synthesis, tricarboxylic acid cycle activity, and metabolic regulation. Supplementary oxidative phosphorylation gene sets were obtained from the Molecular Signatures Database (MSigDB, version 2023.2; https://www.gsea-msigdb.org/) [23], including the *Hallmark Oxidative Phosphorylation* gene set, as well as from curated Reactome pathways (https://reactome.org/) related to mitochondrial respiration and bioenergetics. All mitochondrial gene lists were merged, deduplicated, and standardized to official HGNC gene symbols using the org.Hs.eg.db package (version 3.18.0) [24]. The resulting unified mitochondrial gene panel was defined as mitochondrial genes (MGs) and used for downstream analyses.

2.4 Identification of MG-DEGs

Hub genes within the PPI network were identified using the CytoHubba plugin (version 0.1) in Cytoscape [25]. To improve robustness, genes were ranked using topological algorithms, with Maximal Clique Centrality (MCC) employed as the primary ranking metric. MCC was selected because it has been demonstrated to outperform several traditional centrality measures (e.g., Degree, Betweenness, Closeness) in identifying essential and functionally critical nodes in biological networks. While additional metrics were examined for consistency, final hub gene selection was based primarily on MCC ranking. Functional enrichment analysis of MG-DEGs and identified hub genes was performed using the clusterProfiler package (version 4.8.3) in R [26]. Gene Ontology (GO) enrichment analysis was conducted to identify significantly overrepresented Biological Processes (BP), Cellular Components (CC), and Molecular Functions (MF). Pathway enrichment analysis was performed using KEGG and Reactome databases. Enrichment terms with adjusted p-values < 0.05 (Benjamini-Hochberg correction) were considered statistically significant. Results were visualized using dot plots and enrichment maps to facilitate interpretation of biological relevance.

2.5 PPI Network Construction

To explore functional interactions among MG-DEGs, a PPI network was constructed using the STRING database (version 11.5; https://string-db.org/) [27,28]. MG-DEGs were mapped to STRING, and interactions with a minimum confidence score of 0.4 were retained to balance interaction reliability and network coverage. Both experimentally validated and predicted interactions were included. The interaction network was imported into Cytoscape software (version 3.10.1; https://cytoscape.org/) for visualization and network topology analysis [29-31]. Network connectivity and node interaction patterns were examined to identify key functional clusters.

2.6 Hub Gene Identification and Functional Enrichment Analysis

Hub genes within the PPI network were identified using the CytoHubba plugin (version 0.1) implemented in Cytoscape [32]. Multiple topological algorithms, including Degree and Maximum Clique Centrality (MCC), were applied to rank genes based on their importance within the network. Genes consistently ranked among the top positions were defined as hub genes. Functional enrichment analysis was conducted using the clusterProfiler package (version 4.8.3; https://bioconductor.org/packages/clusterProfiler/) in R [29,33]. GO enrichment analysis was performed to evaluate

overrepresented BP, CC, and MF, while pathway enrichment analysis was conducted using KEGG (https://www.kegg.jp/) and Reactome databases [29,34]. Enrichment terms with adjusted p-values below 0.05 were considered statistically significant and visualized using dot plots and enrichment maps.

2.7 GO Enrichment Analysis

GO enrichment analysis was performed to systematically characterize the BP, cellular localization, and MF associated MG-DEGs [35]. The MG-DEGs were obtained by intersecting the curated mitochondrial gene set with DEGs identified in AML datasets using predefined thresholds (|fold change| > 2 and adjusted p-value < 0.05). GO enrichment analyses for BP, CC, and MF categories were conducted in R (version ≥ 4.2.0) using the clusterProfiler package. Gene identifiers were converted to official HGNC gene symbols and Entrez IDs using the org.Hs.eg.db annotation database. Enrichment was assessed using a hypergeometric test, and p-values were corrected for multiple testing using the Benjamini-Hochberg FDR method. GO terms with an adjusted p-value < 0.05 were considered statistically significant. To enhance biological interpretability, enrichment scores were calculated as -log10 (adjusted p-value), and the top significantly enriched GO terms were selected for visualization. Dot plots were generated using the ggplot2 package to display enriched GO terms, where bubble size represents gene counts and color intensity corresponds to statistical significance. Additionally, gene-term association chord diagrams were constructed using the GOplot and circlize packages to illustrate the relationships between enriched GO categories and contributing genes [36,37]. These visualizations enabled an integrated view of functional pathways and gene participation across major mitochondrial and metabolic processes. All graphical outputs were refined using ComplexHeatmap, ggpubr, and cowplot packages to ensure publication-quality figures [20].

3. Results

3.1 Global Transcriptomic Alterations Induced by Anlotinib in NSCLC Cells

To characterize the global transcriptional impact of Anlotinib in NSCLC, differential gene expression analysis was performed using the GSE237818 dataset, comparing Anlotinib-treated samples with corresponding controls. As shown in Figure 1A, the volcano plot reveals a pronounced transcriptional response, with a large number of genes exhibiting statistically significant differential expression (adjusted $p < 0.05$, $|\log_2 FC| \geq 1$). Both upregulated (red) and downregulated (blue) genes were clearly separated from non-significant transcripts, indicating a robust and well-defined treatment-associated gene expression signature. The distribution of $\log_2$ fold changes across expression intensities was further evaluated using an MA plot (Figure 1B). DEGs were observed across the full spectrum of mean normalized counts, demonstrating that Anlotinib-induced transcriptional changes were not restricted to either low- or high-abundance transcripts. Importantly, fold-change estimates remained stable across expression levels, indicating minimal intensity-dependent bias and supporting the reliability of normalization and statistical modeling. Dispersion estimates generated by DESeq2 are shown in Figure 1C. Gene-wise dispersion values followed the expected inverse relationship with mean expression, and the close concordance between gene-wise estimates, the fitted dispersion trend, and the final dispersion values confirms appropriate modeling of biological variability. This indicates that the dataset possesses sufficient statistical power and low technical noise for downstream analyses. Sample-level quality control further supported the robustness of the dataset. Boxplots of $\log_{10}$-transformed normalized counts (Figure 1D) demonstrated highly consistent expression distributions among biological replicates within each condition, with no evidence of outlier samples or batch-related effects. This confirms strong intra-group reproducibility and validates the dataset for integrative transcriptomic analysis. To investigate the contribution of mitochondrial pathways to the observed transcriptional remodeling, DEGs were intersected with a curated set of mitochondrial and oxidative phosphorylation-related genes. As illustrated in the Venn diagram (Figure 1E), 191 genes overlapped between the Anlotinib-responsive transcriptome and the mitochondrial gene set, defining a distinct subset of MG-DEGs. While the majority of DEGs were non-mitochondrial, the selective enrichment of MG-DEGs suggests targeted modulation of mitochondrial programs rather than global disruption of mitochondrial gene expression. Collectively, these results demonstrate that Anlotinib induces a strong, statistically well-supported transcriptomic response in NSCLC cells, characterized by balanced gene activation and repression, high data quality, and a defined subset of mitochondrial-related genes. This mitochondrial gene signature provides a mechanistic foundation for subsequent network-based and functional enrichment analyses aimed at elucidating how mitochondrial reprogramming contributes to cytoskeletal regulation, ECM remodeling, and enhanced therapeutic vulnerability in NSCLC.

To contextualize the biological relevance of mitochondrial-related genes identified in the Anlotinib-treated NSCLC transcriptomic analysis, their baseline expression patterns were examined across a broad spectrum of normal human tissues and cell types. The heatmap illustrates distinct and gene-specific expression profiles, revealing that many MGs exhibit tissue-dependent expression rather than uniform ubiquitous distribution (Figure 2). Genes involved in core mitochondrial functions, including oxidative phosphorylation, electron transport chain activity, fatty acid metabolism, and redox regulation, displayed consistently higher expression across metabolically active tissues such as liver, kidney, heart, and skeletal muscle, reflecting their elevated bioenergetic demands. Notably, several MGs demonstrated comparatively lower expression in immune cell populations and pluripotent stem cells, suggesting context-dependent mitochondrial utilization linked to cellular differentiation and metabolic state. Conversely, a subset of MGs showed

moderate to high expression across diverse tissue types, underscoring their essential housekeeping roles in maintaining mitochondrial integrity and cellular homeostasis. The observed heterogeneity highlights the functional specialization of mitochondrial gene programs across tissues and reinforces the concept that mitochondrial regulation is tightly coupled to tissue-specific metabolic requirements. Importantly, many MGs dysregulated following Anlotinib treatment in NSCLC cells were found to be highly expressed in normal adult tissues under physiological conditions. This observation suggests that Anlotinib-induced modulation of these genes represents a pathological reprogramming of otherwise tightly regulated mitochondrial pathways. Collectively, this tissue-wide expression analysis provides critical biological context for the MG-DEGs identified in the NSCLC model and supports their functional relevance in energy metabolism, cellular stress responses, and cytoskeletal-metabolic coupling mechanisms implicated in tumor stiffness and drug distribution.

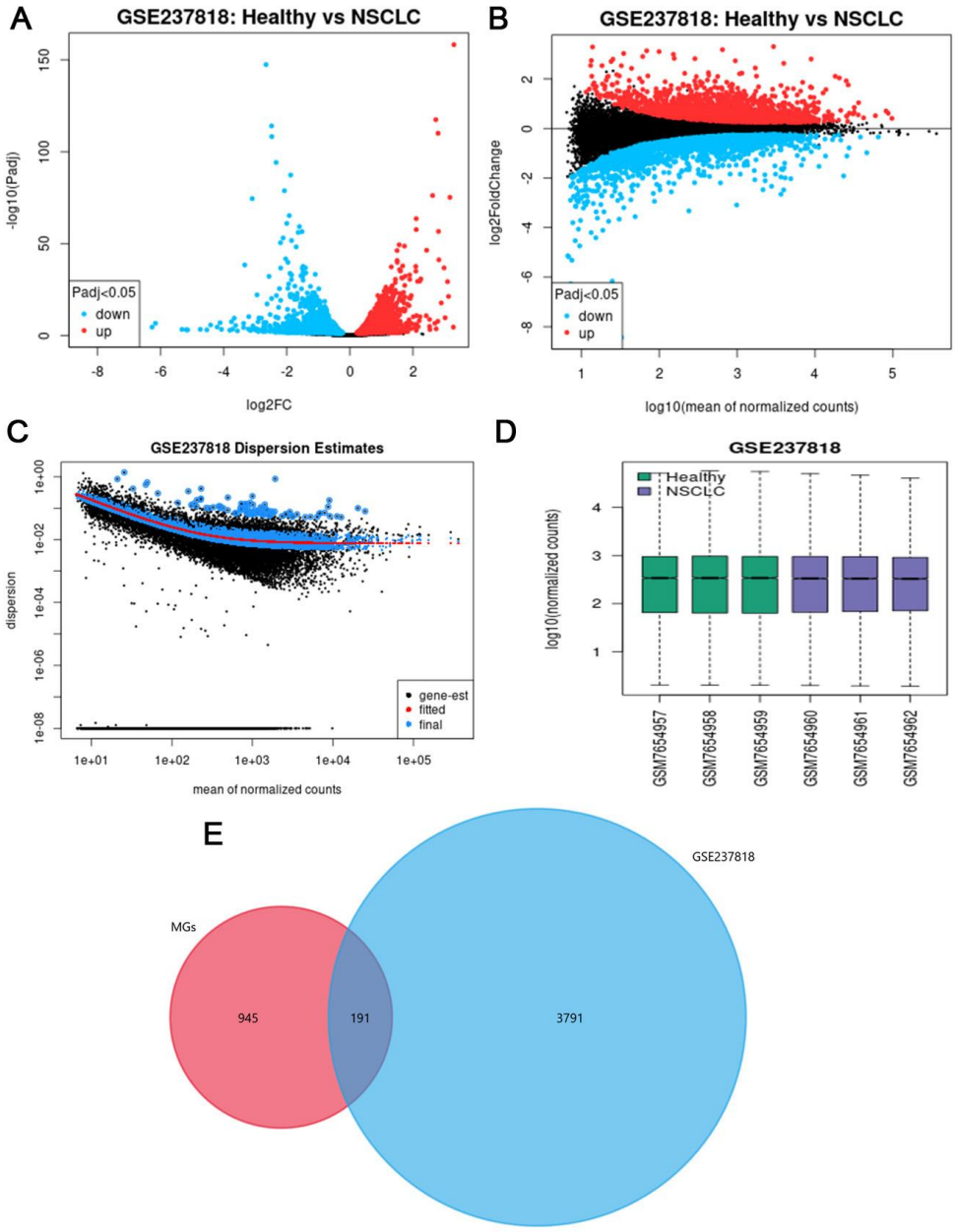

Figure 1. Transcriptomic landscape and identification of MG-DEGs genes in Anlotinib-treated NSCLC cells. (A) Volcano plot showing DEGs between Anlotinib-treated and DMSO-treated A549 NSCLC cells from the GSE237818 dataset. Red dots represent significantly upregulated genes and blue dots represent significantly downregulated genes based on an adjusted p-value < 0.05 and |log2 fold change| ≥ 1. (B) MA plot illustrating the relationship between mean normalized expression levels and log2 fold changes, demonstrating stable variance and minimal expression-dependent bias following normalization. (C) Dispersion estimates generated by DESeq2 showing gene-wise dispersion values, fitted dispersion trend, and final dispersion estimates, indicating appropriate modeling of biological variability across samples. (D) Boxplots of log10-transformed normalized counts for all samples, demonstrating high consistency among biological replicates within control and Anlotinib-treated groups. (E) Venn diagram depicting the overlap between DEGs identified from GSE237818 and curated mitochondrial and oxidative phosphorylation-related genes, highlighting 191 MG-DEGs selected for downstream analyses.

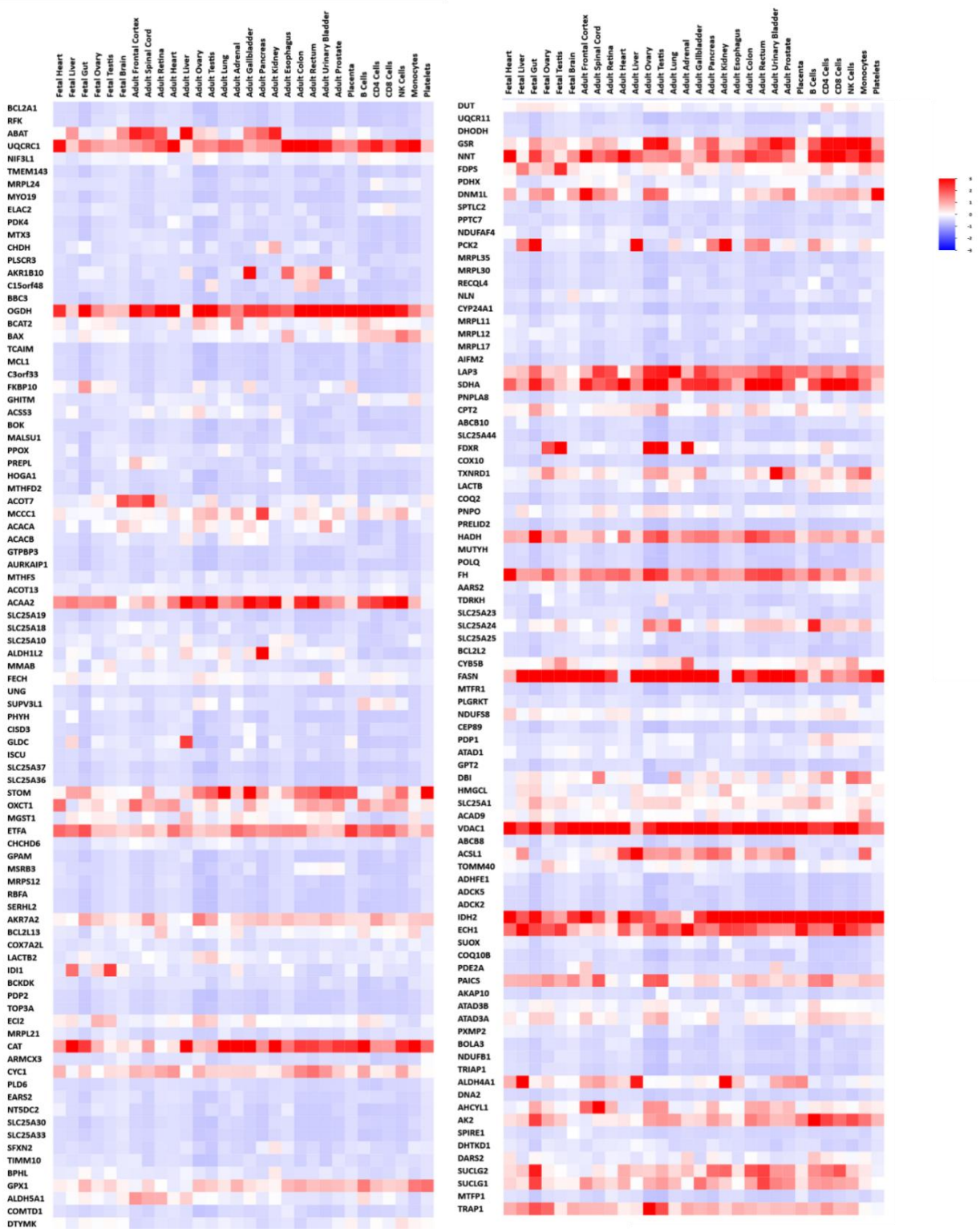

Figure 2. Expression landscape of mitochondrial-related genes across normal human tissues. Heatmap illustrating the relative expression patterns of representative mitochondrial and oxidative phosphorylation-related genes across a broad panel of normal human tissues and cell types. Gene expression values were obtained from publicly available reference transcriptomic datasets and are displayed as row-wise Z-score-normalized expression levels, with red indicating higher expression and blue indicating lower expression. Columns represent distinct fetal and adult tissues, immune cell populations, and pluripotent stem cells, while rows correspond to individual MGs, including those involved in oxidative phosphorylation, mitochondrial metabolism, redox regulation, and apoptotic signaling. This tissue-wide expression profiling provides contextual insight into the baseline distribution and physiological relevance of MGs identified in the Anlotinib-treated NSCLC transcriptomic analysis.

3.2 PPI Network Construction and Hub Gene Identification of MG-DEGs

To elucidate the functional interaction landscape of MG-DEGs, all 191 MG-DEGs identified from the transcriptomic analysis were submitted to the STRING database for PPI analysis. STRING integrates experimentally validated

interactions, curated pathway knowledge, co-expression data, and computational predictions, enabling comprehensive assessment of molecular connectivity. As shown in Figure 3A, the initial STRING-generated PPI network contained both interacting proteins and isolated nodes, reflecting heterogeneous interaction strengths among MGs. To enhance biological interpretability and network robustness, all unconnected (singleton) nodes were removed. This filtering step retained only proteins involved in direct or indirect interactions, yielding a densely interconnected PPI network that more accurately represents coordinated mitochondrial regulatory processes. The refined interaction network is illustrated in Figure 3B, highlighting extensive inter-protein connectivity and suggesting functional cooperation among mitochondrial components. The filtered PPI network was subsequently imported into Cytoscape for advanced visualization and topological analysis. As depicted in Figure 3C, Cytoscape-based layout optimization clearly revealed a highly structured interaction topology, with multiple densely connected clusters indicative of coordinated biological modules. The overall network architecture suggests tight coupling between mitochondrial ribosomal proteins, translational machinery, and mitochondrial stress-response regulators. To identify key regulatory genes within the network, hub gene analysis was performed using the CytoHubba plugin in Cytoscape. Among the available algorithms, the Maximal Clique Centrality (MCC) method was selected due to its superior performance in identifying essential nodes within complex biological networks. Based on MCC scores, the top 10 hub MG-DEGs were identified: *CHCHD1*, *MRPS26*, *MRPS27*, *MRPS17*, *MRPL12*, *MRPL21*, *MRPL28*, *MRPL50*, *GADD45GIP1*, and *AURKAIP1*. These hub genes are visualized as a highly interconnected subnetwork in Figure 3D. Notably, the majority of identified hub genes encode mitochondrial ribosomal proteins (MRPS and MRPL families), underscoring the central role of mitochondrial protein translation in the Anlotinib-induced transcriptional response. The presence of *GADD45GIP1* and *AURKAIP1*, which are implicated in mitochondrial stress signaling, apoptosis, and cell-cycle-associated mitochondrial regulation, further suggests integration between mitochondrial translational control and stress-adaptive pathways. The strong interconnectivity among these hub genes indicates coordinated regulation of mitochondrial ribosome assembly, bioenergetic homeostasis, and mitochondrial quality control. Collectively, these findings demonstrate that Anlotinib-driven transcriptional reprogramming converges on a tightly connected mitochondrial interaction network dominated by translational and stress-response regulators. The identified hub genes represent potential key drivers of mitochondrial dysfunction and therapeutic vulnerability in NSCLC, providing a mechanistic basis for subsequent pathway enrichment, regulatory network, and drug-response analyses.

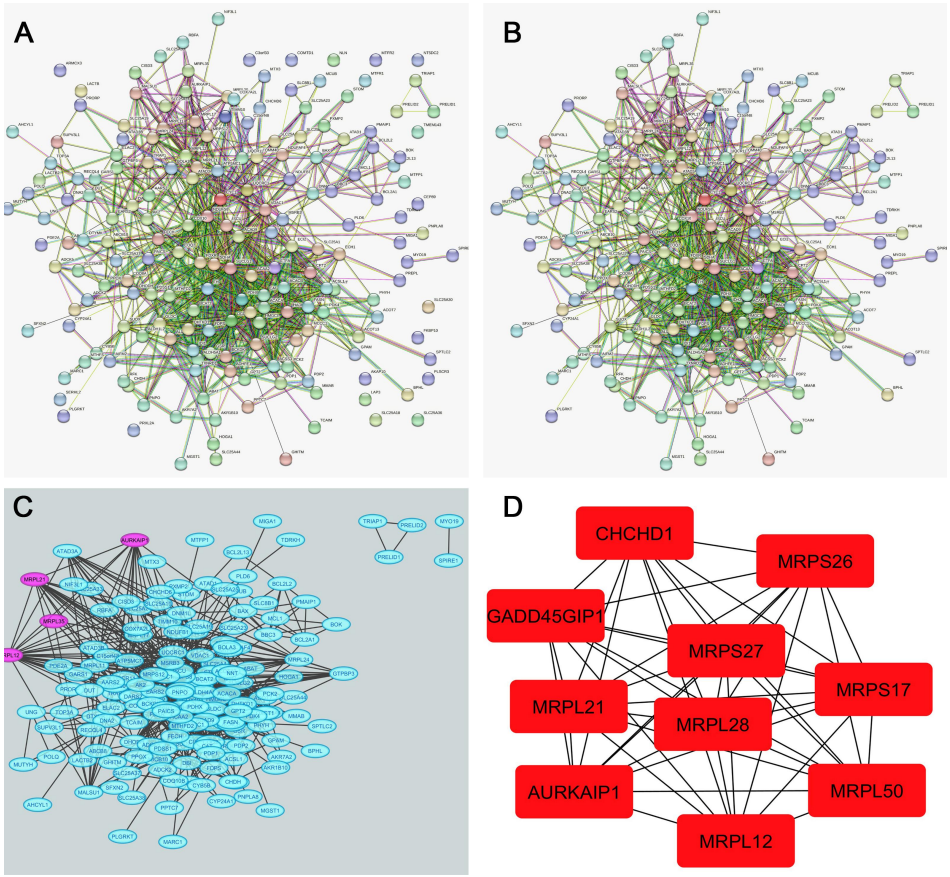

Figure 3. PPI network construction and hub gene identification of MG-DEGs. (A) PPI network generated by submitting 191 MG-DEGs to the STRING database. Nodes represent proteins, and edges indicate predicted or experimentally validated protein-protein interactions. (B) Refined PPI network after removal of unconnected nodes, showing a densely interconnected interaction landscape among MG-DEGs. (C) Cytoscape visualization of the filtered PPI network, illustrating overall network topology and interaction density. (D) Hub gene subnetwork identified using the CytoHubba plugin based on the Maximal Clique Centrality (MCC) algorithm. The top 10 hub MG-DEGs (*CHCHD1*, *MRPS26*, *MRPS27*, *MRPS17*, *MRPL12*, *MRPL21*, *MRPL28*, *MRPL50*, *GADD45GIP1*, and *AURKAIP1*) are highlighted, demonstrating strong interconnectivity and potential key regulatory roles in mitochondrial function.

3.3 Functional Enrichment Analysis of Top MG-DEGs

Across BP, CC, and MF categories, GO enrichment analysis consistently points to extensive metabolic and mitochondrial reprogramming, with coordinated regulation of energy production, mitochondrial architecture, and apoptosis-related mechanisms. These findings provide strong functional evidence that the analyzed gene set plays a critical role in controlling cellular bioenergetics, organelle dynamics, and stress responses, supporting the biological relevance of the observed transcriptomic changes.

GO BP enrichment analysis revealed that the analyzed gene set was strongly associated with energy metabolism, cellular respiration, and metabolic catabolic processes. The most significantly enriched term was generation of precursor metabolites and energy (GO:0006091), involving 39 genes and exhibiting a high enrichment score (23.19) and fold enrichment (7.84), indicating a central role in cellular bioenergetics (Table 1). Key respiration-related processes, including cellular respiration, aerobic respiration, and energy derivation by oxidation of organic compounds, were also highly enriched, underscoring extensive transcriptional modulation of oxidative metabolic pathways (Figure 4). Additionally, pathways related to mitochondrial transport and regulation of mitochondrion organization were significantly overrepresented, suggesting altered mitochondrial dynamics and intracellular trafficking. Notably, multiple catabolic processes Such as carboxylic acid, organic acid, dicarboxylic acid, and small molecule catabolic processes were enriched, reflecting broad metabolic reprogramming. Apoptosis-related processes, including release of cytochrome c from mitochondria and apoptotic mitochondrial changes, further indicate involvement of mitochondrial-mediated cell fate regulation. Collectively, BP enrichment highlights a coordinated regulation of energy metabolism, mitochondrial organization, and apoptotic signaling, consistent with extensive remodeling of cellular bioenergetic and survival pathways.

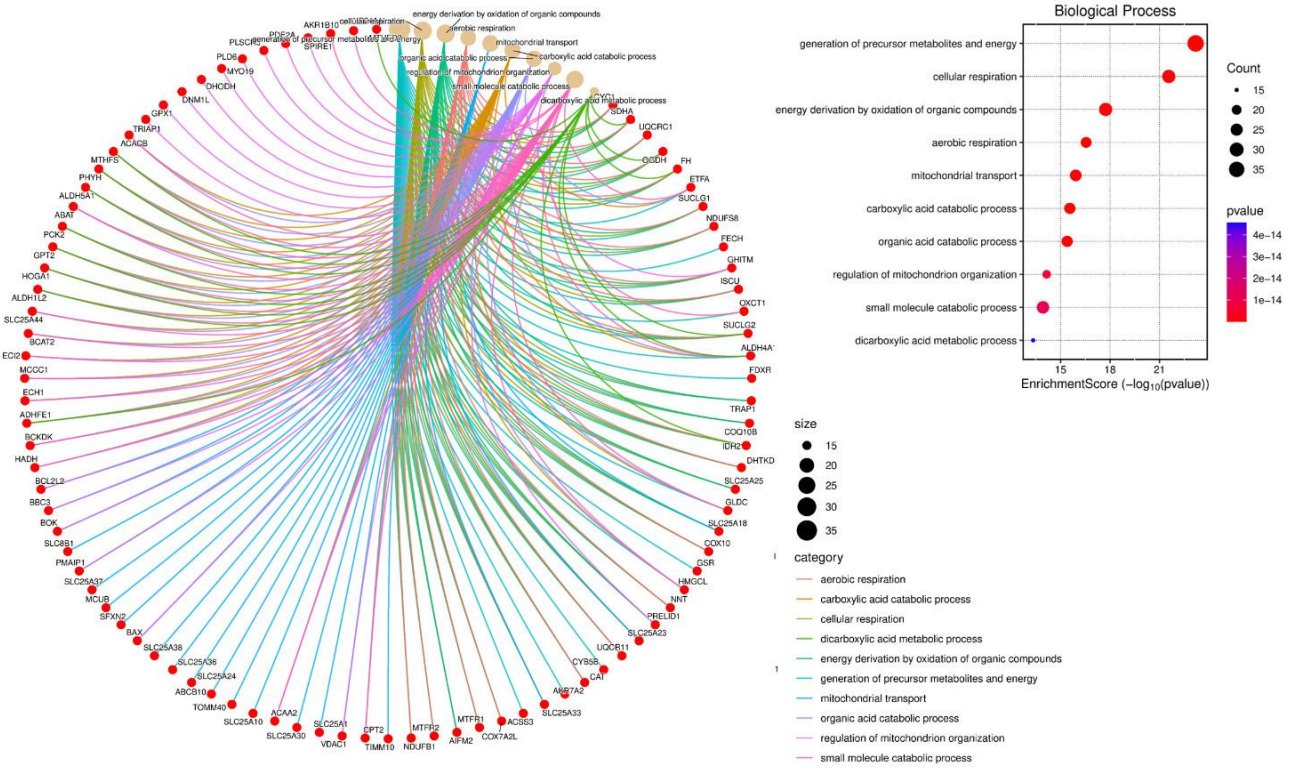

Figure 4. GO BP enrichment analysis of MG-DEGs identified significant overrepresentation of energy metabolism-associated processes. The most enriched terms included generation of precursor metabolites and energy, cellular respiration, aerobic respiration, and energy derivation by oxidation of organic compounds, indicating extensive transcriptional regulation of oxidative metabolic pathways. Additional enrichment was observed in mitochondrial transport, regulation of mitochondrion organization, and multiple catabolic processes, including organic acid, carboxylic acid, dicarboxylic acid, and small-molecule catabolism. Apoptosis-related processes such as release of cytochrome c from mitochondria and apoptotic mitochondrial changes were also significantly enriched. The chord diagram illustrates the relationships between enriched BP terms and their contributing genes, with colored links denoting distinct BP categories. The accompanying bubble plot displays the top enriched BP terms ranked by enrichment score (-log10 adjusted p-value), where bubble size corresponds to gene count and color intensity reflects statistical significance.

Table 1. GO BP enrichment analysis of MG-DEGs.

ID	Description	Gene Ratio	p-Value	Gene ID	Enrich-ment.Score	Fold. Enrichment
GO: 0006091	generation of precursor metabolites and energy	39/ 190	6.48E-24	*CYC1/SDHA/UQCRC1/OGDH/FH/ETFA/SUCLG1/NDUFS8/ FECH/GHITM/ISCU/OXCT1/SUCLG2/ALDH4A1/FDXR/TRA P1/COQ10B/IDH2/DHTKD1/SLC25A25/GLDC/SLC25A18/C OX10/GSR/HMGCL/NNT/PRELID1/SLC25A23/UQCR11/CYB 5B/CAT/AKR7A2/SLC25A33/ACSS3/COX7A2L/MTFR1/AIFM 2/MTFR2/NDUFB1*	23.18816	7.843147
GO: 0045333	cellular respiration	28/ 190	2.74E-22	*CYC1/SDHA/UQCRC1/OGDH/FH/SUCLG1/NDUFS8/GHIT M/ISCU/SUCLG2/TRAP1/COQ10B/IDH2/DHTKD1/SLC25A2 5/SLC25A18/COX10/NNT/PRELID1/SLC25A23/UQCR11/CAT /SLC25A33 /COX7A2L/MTFR1/AIFM2/MTFR2/NDUFB1*	21.56159	11.99643
GO: 0015980	energy derivation by oxidation of organic compounds	28/ 190	1.84E-18	*CYC1/SDHA/UQCRC1/OGDH/FH/SUCLG1/NDUFS8/GHIT M/ISCU/SUCLG2/TRAP1/COQ10B/IDH2/DHTKD1/SLC25A2 5/SLC25A18/COX10/NNT/PRELID1/SLC25A23/UQCR11/CAT /SLC25A33/COX7A2L/MTFR1/AIFM2/MTFR2/NDUFB1*	17.73414	8.676663
GO: 0009060	aerobic respiration	22/ 190	2.81E-17	*CYC1/SDHA/UQCRC1/OGDH/FH/SUCLG1/NDUFS8/GHIT M/ISCU/SUCLG2/IDH2/DHTKD1/COX10/NNT/SLC25A23/U QCR11/CAT/SLC25A33/COX7A2L/MTFR1/MTFR2/NDUFB1*	16.55192	11.47051
GO: 0006839	mitochondrial transport	24/19 0	1.2E-16	*TIMM10/CPT2/VDAC1/SLC25A1/SLC25A30/ACAA2/SLC25A 10/TOMM40/ABCB10/SLC25A24/SLC25A18/SLC25A23/SLC2 5A36/SLC25A38/SLC25A33/BAX/SFXN2/MCUB/SLC25A37/P MAIP1/SLC8B1/BOK/BBC3/BCL2L2*	15.92158	9.311065
GO: 0046395	carboxylic acid catabolic process	23/ 190	2.72E-16	*ETFA/CPT2/HADH/BCKDK/ADHFE1/ECH1/ALDH4A1/MCC C1/ACAA2/GLDC/ECI2/BCAT2/HMGCL/SLC25A44/ALDH1L 2/HOGA1/GPT2/PCK2/ABAT/ALDH5A1/PHYH/MTHFS/ACA CB*	15.56477	9.60368
GO: 0016054	organic acid catabolic process	23/ 190	3.95E-16	*ETFA/CPT2/HADH/BCKDK/ADHFE1/ECH1/ALDH4A1/MCC C1/ACAA2/GLDC/ECI2/BCAT2/HMGCL/SLC25A44/ALDH1L 2/HOGA1/GPT2/PCK2/ABAT/ALDH5A1/PHYH/MTHFS/ACA CB*	15.40364	9.443618
GO: 0010821	regulation of mitochondrion organization	18/ 190	6.93E-15	*GHITM/VDAC1/ACAA2/TRIAP1/GPX1/PRELID1/BAX/DNM1 L/DHODH/PMAIP1/MYO19/PLD6/PLSCR3/BOK/BBC3/BCL 2L2/PDE2A/SPIRE1*	14.15935	12.31776
GO: 0044282	small molecule catabolic process	26/19 0	1.15E-14	*ETFA/CPT2/HADH/BCKDK/ADHFE1/OXCT1/ECH1/ALDH4 A1/MCCC1/ACAA2/GLDC/ECI2/BCAT2/HMGCL/SLC25A44/ ALDH1L2/HOGA1/GPT2/PCK2/ABAT/ALDH5A1/AKR1B10/P HYH/MTHFS/ACACB/CYP24A1*	13.93829	6.814082
GO: 0043648	dicarboxylic acid metabolic process	15/ 190	4.55E-14	*SDHA/OGDH/FH/ADHFE1/SUCLG2/ALDH4A1/IDH2/MTHF D2/ALDH1L2/HOGA1/GPT2/PCK2/ALDH5A1/PHYH/MTHFS*	13.34163	15.3972
GO: 0022900	electron transport chain	17/ 190	2.63E-12	*CYC1/SDHA/UQCRC1/ETFA/NDUFS8/GHITM/ISCU/ALDH4 A1/GLDC/SLC25A18/GSR/UQCR11/CYB5B/AKR7A2/COX7A 2L/AIFM2/NDUFB1*	11.57979	9.572662
GO: 0001836	release of cytochrome c from mitochondria	11/ 190	1.61E-11	*GHITM/TRIAP1/GPX1/PRELID1/BAX/DNM1L/PMAIP1/PLS CR3/BOK/BBC3/BCL2L2*	10.79325	18.37226
GO: 1990542	mitochondrial transmembrane transport	13/ 190	3.41E-11	*CPT2/VDAC1/SLC25A1/TOMM40/SLC25A18/SLC25A23/SLC 25A36/SLC25A38/SLC25A33/SFXN2/MCUB/SLC25A37/SLC8 B1*	10.46774	12.55929
GO: 0090199	regulation of release of cytochrome c from mitochondria	10/ 190	4.28E-11	*GHITM/TRIAP1/GPX1/PRELID1/BAX/DNM1L/PMAIP1/PLS CR3/BBC3/BCL2L2*	10.36904	20.52961
GO: 0008637	apoptotic mitochondrial changes	13/ 190	6.31E-11	*GHITM/ACAA2/TRIAP1/GPX1/PRELID1/BAX/DNM1L/AIFM 2/PMAIP1/PLSCR3/BOK/BBC3/BCL2L2*	10.19983	11.97241
GO: 0009117	nucleotide metabolic process	24/ 190	1.82E-10	*OGDH/PDK4/PDHX/SUCLG2/SLC25A1/IDH2/DHTKD1/AK2 /HMGCL/ACACA/RFK/DUT/GARS1/ACACB/ACSL1/DTYMK/ FASN/ACOT7/UNG/ATP5MC1/DHODH/GPAM/PAICS/PDE2 A*	9.740627	4.836422
GO: 1901661	quinone metabolic process	9/ 190	1.97E-10	*PPTC7/COQ8A/FDXR/COQ10B/COQ2/PDSS1/AKR1B10/AK R7A2/AIFM2*	9.706076	22.17197
GO: 0006637	acyl-CoA metabolic process	12/ 190	2.5E-10	*OGDH/PDK4/PDHX/SUCLG2/SLC25A1/HMGCL/ACACA/AC ACB/ACSL1/FASN/A COT7/GPAM*	9.601978	12.31776
GO: 0035383	thioester metabolic process	12/ 190	2.5E-10	*OGDH/PDK4/PDHX/SUCLG2/SLC25A1/HMGCL/ACACA/AC ACB/ACSL1/FASN/ACOT7/GPAM*	9.601978	12.31776
GO: 0006753	nucleoside phosphate metabolic process	24/ 190	2.53E-10	*OGDH/PDK4/PDHX/SUCLG2/SLC25A1/ID H2/DHTKD1/AK2/HMGCL/ACACA/RFK/DUT/GARS1/ACAC B/ACSL1/DTYMK/FASN/ACOT7/UNG/ATP5MC1/DHODH/G PAM/PAICS/PDE2A*	9.597643	4.758572

3.4 GO Cellular Component Enrichment Analysis

CC enrichment analysis demonstrated a pronounced localization of the gene set to mitochondrial structures. The most significantly enriched term was mitochondrial matrix (GO: 0005759), with 63 genes and an exceptionally high enrichment score (53.20), indicating strong mitochondrial compartment specificity (Figure 5). Additional highly enriched components included the mitochondrial inner membrane, mitochondrial protein-containing complexes, and mitochondrial outer membrane, emphasizing widespread involvement across mitochondrial subcompartments. Enrichment of the respirasome and electron transport chain-associated complexes further supports functional participation in oxidative phosphorylation machinery (Table 2). Interestingly, enrichment was also observed for peroxisome and microbody components, suggesting potential metabolic crosstalk between mitochondria and other oxidative organelles. The presence of genes associated with the organelle envelope lumen and intermembrane space reflects alterations in mitochondrial transport, protein import, and apoptotic signaling hubs. Importantly, no cytoskeletal, focal adhesion, ECM, or RhoA/ROCK-related cellular component terms were significantly enriched within the MG-DEG subset. Overall, CC analysis confirms that the analyzed genes are predominantly localized to mitochondrial membranes, matrix, and respiratory complexes, reinforcing the centrality of mitochondrial architecture in the observed transcriptional landscape.

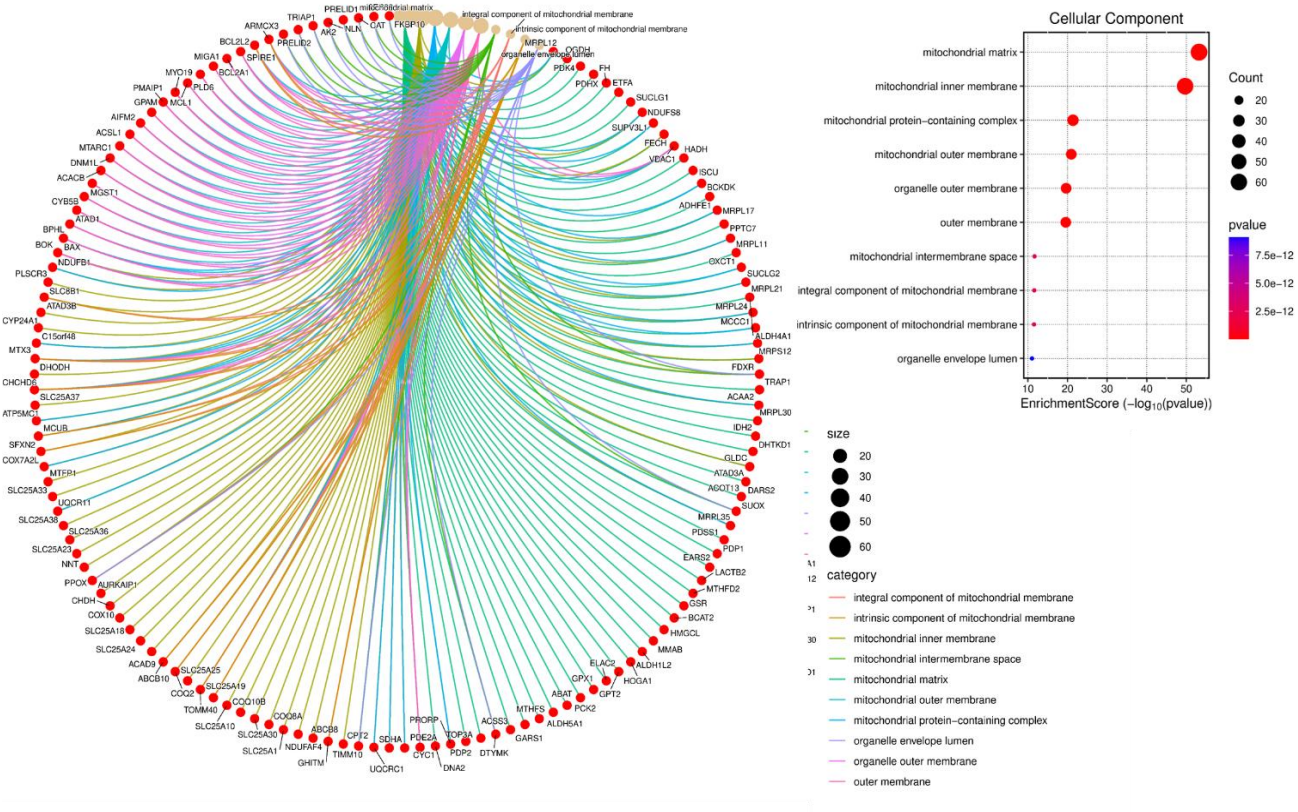

Figure 5. GO-CC enrichment analysis revealed strong localization of MG-DEGs to mitochondrial subcellular compartments. The most significantly enriched terms included the *mitochondrial matrix*, *mitochondrial inner membrane*, *mitochondrial outer membrane*, and *mitochondrial protein-containing complexes*, highlighting broad involvement across mitochondrial architecture. Enrichment of respiratory chain-associated structures, including the *respirasome* and *electron transport chain complexes*, supports functional participation in oxidative phosphorylation machinery. Additional enrichment in the intermembrane space and organelle envelope lumen suggests roles in mitochondrial transport, protein import, and apoptotic signaling. Bubble size represents the number of genes enriched in each component, while color indicates the adjusted p-value, reflecting the strength of statistical enrichment.

Table 2 summarizes significantly enriched GO-CC terms associated with the top MG-DEGs. ID represents the GO accession number; Description indicates the name of the enriched cellular component; BgRatio denotes the ratio of genes annotated to the term in the background gene set; p value represents the statistical significance of enrichment; Gene ID lists the MG-DEGs involved in each GO term; and Fold Enrichment indicates the magnitude of enrichment compared to the background distribution.

Table 2. GO-CC enrichment analysis of the top MG-DEGs.

ID: GO	Description	Bg Ratio	p-value	Gene ID	Fold. Enrichment
0005759	mitochondrial matrix	480/ 19550	6.34335E-54	*MRPL12/OGDH/PDK4/PDHX/FH/ETFA/SUCLG1/NDUFS8/SUPV3L1/FECH/VDAC1/HADH/ISCU/BCKDK/ADHFE1/MRPL17/PPTC7/MRPL11/XCT1/SUCLG2/MRPL21/ALDH4A1/MRPL24/MCCC1/MRPS12/FDXR/TRAP1/ACAA2/MRPL30/IDH2/DHTKD1/GLDC/ATAD3A/DARS2/ACOT13/SUOX/MRPL35/PDSS1/PDP1/EARS2/LACTB2/MTHFD2/GSR/BCAT2/HMGCL/MMAB/ALDH1L2/HOGA1/GPT2/ELAC2/GPX1/PCK2/ABAT/ALDH5A1/MTHFS/GARS1/ACSS3/DTYMK/TOP3A/PDP2/PRORP/DNA2/PDE2A*	13.50493421
0005743	mitochondrial inner membrane	495/ 19550	2.06675E-50	*CYC1/SDHA/UQCRC1/MRPL12/TIMM10/CPT2/NDUFS8/FECH/GHITM/ABCB8/NDUFAF4/MRPL17/MRPL11/SLC25A1/MRPL21/COQ8A/MRPL24/MRPS12/SLC25A30/FDXR/TRAP1/MRPL30/COQ10B/SLC25A10/SLC25A19/TOMM40/SLC25A25/ATAD3A/COQ2/ABCB10/ACAD9/SLC25A24/SLC25A18/COX10/MRPL35/CHDH/AURKAIP1/PPOX/NNT/SLC25A23/SLC25A36/SLC25A38/UQCR11/SLC25A33/MTFP1/COX7A2L/SFXN2/MCUB/ATP5MC1/SLC25A37/CHCHD6/DHODH/MTX3/C15orf48/CYP24A1/ATAD3B/SLC8B1/PLSCR3/NDUFB1/BOK/PDE2A*	12.67995747
0098798	mitochondrial protein-containing complex	268/ 19550	4.20064E-22	*CYC1/SDHA/UQCRC1/MRPL12/TIMM10/NDUFS8/SUPV3L1/VDAC1/BCKDK/MRPL17/MRPL11/SUCLG2/MRPL21/MRPL24/MCCC1/MRPS12/MRPL30/TOMM40/MRPL35/UQCR11/BAX/COX7A2L/MCUB/ATP5MC1/CHCHD6/MTX3/C15orf48/PRORP/NDUFB1*	11.13413197
0005741	mitochondrial outer membrane	205/ 19550	1.13229E-21	*VDAC1/BPHL/TOMM40/ATAD1/CYB5B/MGST1/BAX/ACACB/DNM1L/MTARC1/ACSL1/CHCHD6/MTX3/AIFM2/GPAM/PMAIP1/MYO19/MCL1/PLD6/BOK/MIGA1/BCL2A1/BCL2L2/PDE2A/SPIRE1/ARMCX3*	13.05006418
0031968	organelle outer membrane	230/ 19550	2.21688E-20	*VDAC1/BPHL/TOMM40/ATAD1/CYB5B/MGST1/BAX/ACACB/DNM1L/MTARC1/ACSL1/CHCHD6/MTX3/AIFM2/GPAM/PMAIP1/MYO19/MCL1/PLD6/BOK/MIGA1/BCL2A1/BCL2L2/PDE2A/SPIRE1/ARMCX3*	11.63157895
0019867	outer membrane	232/ 19550	2.76766E-20	*VDAC1/BPHL/TOMM40/ATAD1/CYB5B/MGST1/BAX/ACACB/DNM1L/MTARC1/ACSL1/CHCHD6/MTX3/AIFM2/GPAM/PMAIP1/MYO19/MCL1/PLD6/BOK/MIGA1/BCL2A1/BCL2L2/PDE2A/SPIRE1/ARMCX3*	11.53130672
0005758	mitochondrial intermembrane space	86/ 19550	2.13858E-12	*TIMM10/TRAP1/PRELID2/SUOX/TRIAP1/AK2/NLN/PPOX/PRELID1/CAT/DTYMK/CEP89/FKBP10*	15.55385557
0032592	integral component of mitochondrial membrane	87/ 19550	2.49312E-12	*GHITM/SLC25A19/TOMM40/COQ2/ABCB10/PPOX/SFXN2/MCUB/CHCHD6/MTX3/SLC8B1/SPIRE1/ARMCX3*	15.37507562
0098573	intrinsic component of mitochondrial membrane	88/ 19550	2.90064E-12	*GHITM/SLC25A19/TOMM40/COQ2/ABCB10/PPOX/SFXN2/MCUB/CHCHD6/MTX3/SLC8B1/SPIRE1/ARMCX3*	15.20035885
0031970	organelle envelope lumen	96/ 19550	9.11406E-12	*TIMM10/TRAP1/PRELID2/SUOX/TRIAP1/AK2/NLN/PPOX/PRELID1/CAT/DTYMK/CEP89/FKBP10*	13.93366228
0005777	peroxisome	142/ 19550	1.12152E-10	*ECH1/IDH2/ECI2/ATAD1/PNPLA8/HMGCL/PXMP2/PHYH/CAT/MGST1/DNM1 L/ACSL1/IDI1/SERHL2*	10.14455152
0042579	microbody	142/ 19550	1.12152E-10	*ECH1/IDH2/ECI2/ATAD1/PNPLA8/HMGCL/PXMP2/PHYH/CAT/MGST1/DNM 1L/ACSL1/IDI1/SERHL2*	10.14455152
1990204	oxidoreductase complex	112/ 19550	9.48831E-10	*CYC1/SDHA/UQCRC1/OGDH/PDHX/NDUFS8/BCKDK/GLDC/UQCR11/CYB5B/ MTARC1/NDUFB1*	11.02443609
0098800	inner mitochondrial membrane protein complex	147/ 19550	2.04248E-09	*CYC1/SDHA/UQCRC1/TIMM10/NDUFS8/UQCR11/COX7A2L/MCUB/ATP5MC1/CHCHD6/MTX3/C15orf48/NDUFB1*	9.099534551
0031304	intrinsic component of mitochondrial inner membrane	56/ 19550	6.54655E-08	*GHITM/SLC25A19/COQ2/PPOX/SFXN2/MCUB/CHCHD6/MTX3*	14.69924812
0031305	integral component of mitochondrial inner membrane	56/ 19550	6.54655E-08	*GHITM/SLC25A19/COQ2/PPOX/SFXN2/MCUB/CHCHD6/MTX3*	14.69924812
0045239	tricarboxylic acid cycle enzyme complex	13/ 19550	9.938E-08	*OGDH/FH/SUCLG1/BCKDK/SUCLG2*	39.57489879
0005746	mitochondrial respirasome	89/ 19550	2.08236E-07	*CYC1/SDHA/UQCRC1/NDUFS8/NNT/UQCR11/COX7A2L/C15orf48/NDUFB1*	10.40508575
0070469	respirasome	100/ 19550	5.68558E-07	*CYC1/SDHA/UQCRC1/NDUFS8/NNT/UQCR11/COX7A2L/C15orf48/NDUFB1*	9.260526316
0000315	organellar large ribosomal subunit	54/19 550	8.82651E-07	*MRPL12/MRPL17/MRPL11/MRPL21/MRPL24/MRPL30/MRPL35*	13.33820663

Molecular Function enrichment analysis revealed that the gene set was functionally enriched in enzymatic activities and binding functions essential for redox balance, metabolite transport, and apoptosis regulation. The most significant MF terms included vitamin binding, electron transfer activity, and oxidoreductase activity, highlighting involvement in redox reactions and cofactor-dependent metabolism (Figure 6). Notably, BH domain binding exhibited exceptionally high fold enrichment (> 50), indicating a strong association with BCL-2 family proteins and mitochondrial apoptosis regulation (Table 3). Enrichment of nucleotide and organic anion transmembrane transporter activity reflects active mitochondrial solute exchange, particularly mediated by the SLC25 family. Additional enriched functions included fatty-acyl-CoA binding, acyl-CoA binding, and iron-sulfur cluster binding, underscoring roles in lipid metabolism, electron transport, and enzymatic catalysis. Functions related to ATP transmembrane transporter activity further support altered mitochondrial energy exchange. Together, MF enrichment indicates a functional profile dominated by redox metabolism, mitochondrial transport, lipid handling, and apoptosis-associated molecular interactions, consistent with the BP and CC findings.

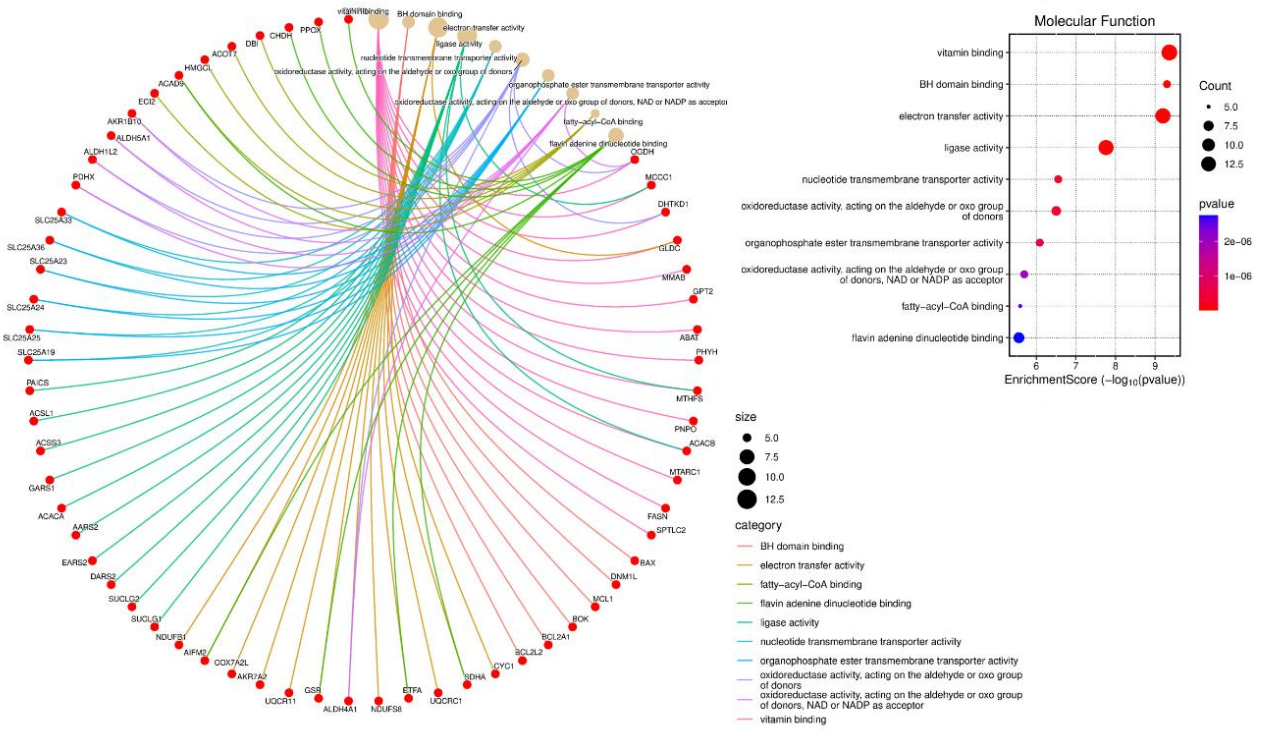

Figure 6. GO-MF enrichment analysis demonstrated that MG-DEGs. Analysis demonstrated that MG-DEGs were primarily associated with enzymatic activities and binding functions essential for redox regulation, metabolism, and mitochondrial transport. Significantly enriched functions included electron transfer activity, oxidoreductase activity, and vitamin and cofactor binding, underscoring involvement in redox homeostasis and cofactor-dependent metabolic reactions. Notably, BH domain binding showed exceptionally high fold enrichment, indicating strong association with BCL-2 family proteins and mitochondrial apoptosis regulation. Enrichment of nucleotide and organic anion transmembrane transporter activity, largely mediated by SLC25 family members, highlights altered mitochondrial solute exchange. Enrichment scores are shown on the x-axis, with dot size indicating gene count and color representing adjusted p-value significance.

Table 3 presents significantly enriched GO-MF terms associated with the top MG-DEGs. ID indicates the GO accession number; Description represents the name of the enriched molecular function; Gene Ratio refers to the proportion of MG-DEGs involved in a specific GO term relative to the total number of input genes; p.adjust denotes the adjusted p-value after multiple testing correction (Benjamini-Hochberg method); Gene ID lists the MG-DEGs contributing to each term; Enrichment Score reflects the significance level of enrichment; and Fold Enrichment indicates the magnitude of overrepresentation compared with the background gene set.

Table 3. GO-MF enrichment analysis of the top MG-DEGs.

ID	Description	Gene Ratio	p. Adjust	Gene ID	Enrichment. Score	Fold. Enrichment
GO: 0019842	vitamin binding	14/190	7.55E-08	*OGDH/MCCC1/DHTKD1/GLDC/MMAB/GPT2/ABAT/PHYH/MTHFS/PNPO/ACACB/MTARC1/FASN/SPTLC2*	9.361053	9.144808
GO: 0051400	BH domain binding	6/190	7.55E-08	*BAX/DNM1L/MCL1/BOK/BCL2A1/BCL2L2*	9.300202	52.7311
GO: 0009055	electron transfer activity	13/190	7.55E-08	*CYC1/SDHA/UQCRC1/ETFA/NDUFS8/ALDH4A1 /GLDC/GSR/UQCR11/AKR7A2/COX7A2L/AIFM2/NDUFB1*	9.19864	9.974269
GO: 0016874	ligase activity	13/190	1.55E-06	*SUCLG1/SUCLG2/MCCC1/DARS2/EARS2/AARS2/ACACA/MTHFS/GARS1/ACACB/ACSS3/ACSL1/PAICS*	7.761008	7.616715
GO: 0015215	nucleotide transmembrane transporter activity	6/190	1.88E-05	*SLC25A19/SLC25A25/SLC25A24/SLC25A23/SLC25A36/SLC25A33*	6.553377	21.48304
GO: 0016903	oxidoreductase activity, acting on the aldehyde or oxo group of donors	7/190	1.88E-05	*OGDH/PDHX/ALDH4A1/DHTKD1/ALDH1L2/ALDH5A1/AKR1B10*	6.502298	15.3799
GO: 0015605	organophosphate ester transmembrane transporter activity	6/190	4.19E-05	*SLC25A19/SLC25A25/SLC25A24/SLC25A23/ SLC25A36/SLC25A33*	6.086136	18.12632
GO: 0016620	oxidoreductase activity, acting on the aldehyde or oxo group of donors, NAD or NADP as acceptor	6/190	9.02E-05	*OGDH/PDHX/ALDH4A1/ALDH1L2/ALDH5A1/AKR1B10*	5.695633	15.67681
GO: 0000062	fatty-acyl-CoA binding	5/190	9.87E-05	*ECI2/ACAD9/HMGCL/ACOT7/DBI*	5.590975	21.97129
GO: 0050660	flavin adenine dinucleotide binding	8/190	9.87E-05	*SDHA/ETFA/ACAD9/CHDH/GSR/PPOX/ TXNRD1/AIFM2*	5.559509	9.0987
GO: 1901567	fatty acid derivative binding	5/190	0.000106	*ECI2/ACAD9/HMGCL/ACOT7/DBI*	5.488169	21.01602
GO: 0120227	acyl-CoA binding	5/190	0.000151	*ECI2/ACAD9/HMGCL/ACOT7/DBI*	5.297097	19.33474
GO: 0051536	iron-sulfur cluster binding	7/190	0.000165	*NDUFS8/FECH/ISCU/CISD3/ABAT/MUTYH/DNA2*	5.190072	9.951703
GO: 0051540	metal cluster binding	7/190	0.000165	*NDUFS8/FECH/ISCU/CISD3/ABAT/MUTYH/DNA2*	5.190072	9.951703
GO: 0015932	nucleobase-containing compound transmembrane transporter activity	6/190	0.000294	*SLC25A19/SLC25A25/SLC25A24/SLC25A23/SLC25A36/SLC25A33*	4.909323	11.60084
GO: 0030170	pyridoxal phosphate binding	6/190	0.000451	*GLDC/GPT2/ABAT/PNPO/MTARC1/SPTLC2*	4.666833	10.54622
GO: 0008514	organic anion transmembrane transporter activity	10/190	0.000451	*SLC25A1/SLC25A30/SLC25A10/SLC25A19/SLC25A25/SLC25A24/SLC25A18/SLC25A23/SLC25A38/SFXN2*	4.63077	5.225605
GO: 0004659	prenyltransferase activity	4/190	0.000451	*COQ2/COX10/PDSS1/FDPS*	4.624165	22.74675
GO: 0070279	vitamin B6 binding	6/190	0.000451	*GLDC/GPT2/ABAT/PNPO/MTARC1/SPTLC2*	4.621335	10.35789
GO: 0016765	transferase activity, transferring alkyl or aryl (other than methyl) groups	6/190	0.000525	*COQ2/COX10/PDSS1/MMAB/MGST1/FDPS*	4.533045	10.00073

3.5 KEGG Pathway Enrichment Reveals Mitochondrial Metabolic Reprogramming Following Anlotinib Treatment

To elucidate the functional consequences of Anlotinib-induced mitochondrial transcriptional remodeling in NSCLC cells, KEGG pathway enrichment analysis was performed on the 191 MG-DEGs. The analysis revealed a strong and highly significant enrichment of pathways governing mitochondrial energy metabolism, oxidative phosphorylation, and redox homeostasis, highlighting mitochondria as a central target of Anlotinib action. Among the most significantly enriched pathways, the citrate cycle (TCA cycle; hsa00020) emerged as the top pathway (adjusted $p = 6.78 \times 10^{-6}$; fold enrichment = 19.75), involving key mitochondrial enzymes including *SDHA*, *OGDH*, *FH*, *SUCLG1*, *SUCLG2*, and

IDH2 (Figure 7A). This finding indicates a profound reprogramming of mitochondrial carbon flux and bioenergetic capacity in response to Anlotinib (Figure 7). Consistently, multiple interconnected metabolic pathways were significantly enriched, including carbon metabolism (hsa01200) (Figure 7B), 2-oxocarboxylic acid metabolism (hsa01210), and one-carbon pool by folate (hsa00670), underscoring coordinated regulation of mitochondrial substrate utilization and biosynthetic processes. Enrichment of valine, leucine and isoleucine degradation (hsa00280) and propanoate metabolism (hsa00640) further suggests enhanced mitochondrial amino acid catabolism and anaplerotic input into the TCA cycle. Importantly, pathways directly linked to mitochondrial respiration were prominently represented. Oxidative phosphorylation (hsa00190) and thermogenesis (hsa04714) were significantly enriched, driven by the differential expression of electron transport chain components such as *CYC1*, *SDHA*, *UQCRC1*, *NDUFS8*, *COX10*, *ATP5MC1*, and *NDUFB1*. These results indicate that Anlotinib alters mitochondrial respiratory chain organization and ATP production efficiency. Lipid metabolism-related pathways, including fatty acid biosynthesis (hsa00061), fatty acid metabolism (hsa01212), and fatty acid degradation (hsa00071), were also significantly enriched, reflecting a shift in mitochondrial lipid handling that may influence membrane composition, mitochondrial dynamics, and bioenergetic flexibility. Additionally, enrichment of the peroxisome pathway (hsa04146) suggests coordinated regulation between mitochondrial and peroxisomal metabolic processes (Figure 7C).

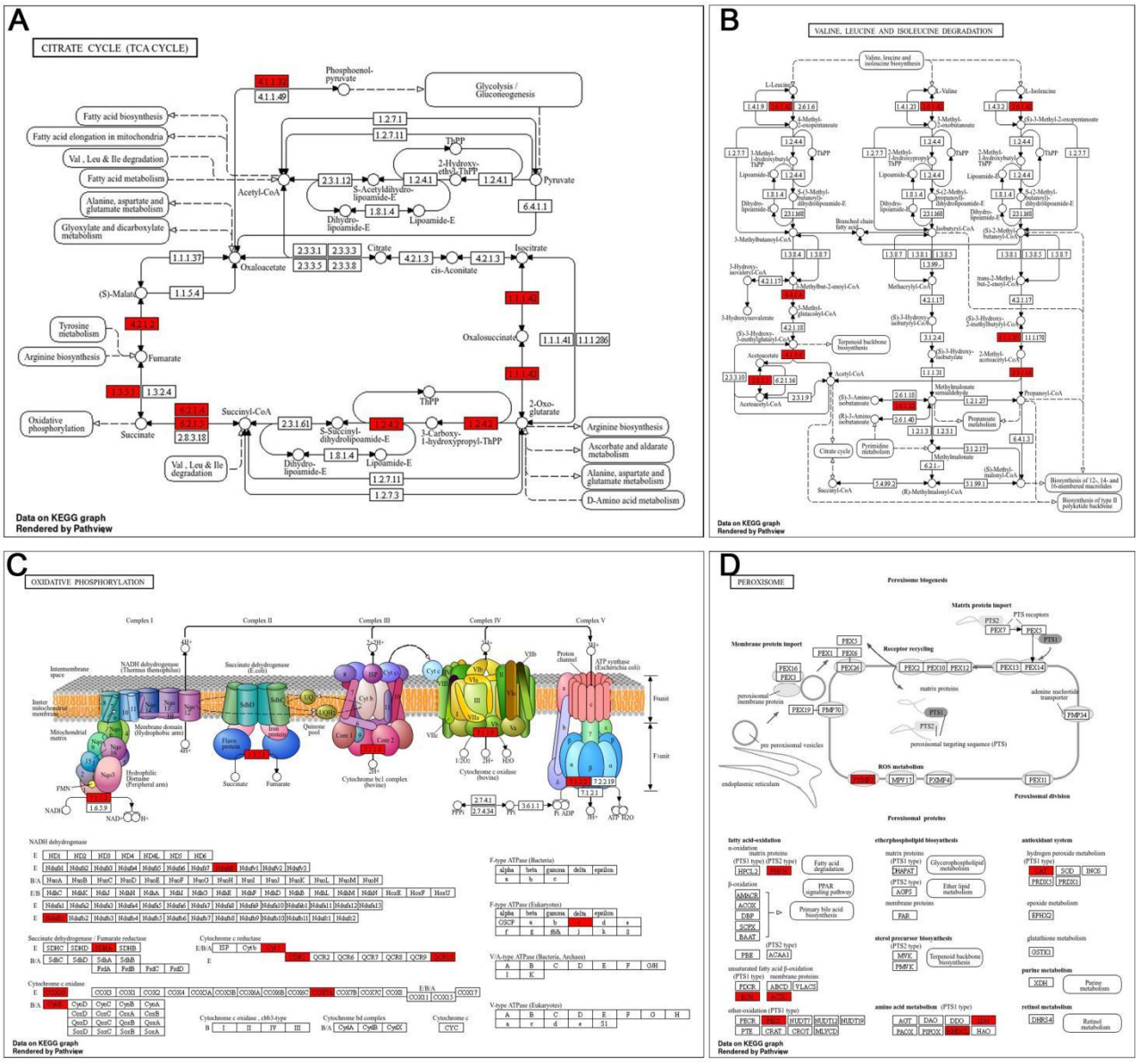

Figure 7. KEGG pathway enrichment analysis MG-DEGs following Anlotinib treatment in NSCLC cells. Integrated KEGG pathway enrichment analysis showing significantly regulated genes involved in (A) Citrate cycle (TCA cycle), (B) Valine, leucine and isoleucine degradation. (C) Oxidative phosphorylation. (D) Peroxisome metabolism, where red-highlighted nodes indicate differentially expressed genes associated with mitochondrial energy metabolism, amino-acid catabolism, and oxidative stress regulation.

Notably, several disease-associated pathways–such as diabetic cardiomyopathy (hsa05415), Parkinson disease (hsa05012), Huntington disease (hsa05016), and amyotrophic lateral sclerosis (hsa05014)–were enriched (Figure 7D).

These pathways are well recognized for their strong mitochondrial involvement, reinforcing the biological relevance of the observed mitochondrial perturbations. Apoptosis-related signaling was also evident, as indicated by enrichment of apoptosis-multiple species (hsa04215), involving pro-apoptotic mitochondrial regulators including *BAX*, *PMAIP1*, *BOK*, and *BBC3*, suggesting that mitochondrial metabolic stress may sensitize NSCLC cells to apoptotic cues following Anlotinib treatment. Importantly, canonical cytoskeletal and mechanotransduction pathways such as "Regulation of actin cytoskeleton," "Focal adhesion," or "ECM-receptor interaction" were not among the top significantly enriched KEGG pathways within the MG-DEG subset. Moreover, key RhoA/ROCK pathway genes (e.g., *RHOA*, *ROCK1*, *ROCK2*, *MYL9*) were not identified as significantly differentially expressed in this analysis. Crucially, many of the enriched KEGG pathways were driven by genes overlapping with the top-10 hub genes identified by CytoHubba (MCC algorithm), particularly mitochondrial ribosomal and respiratory genes such as *MRPL12*, *MRPL21*, *MRPL28*, *MRPL50*, *MRPS17*, *MRPS26*, *MRPS27*, *CHCHD1*, *GADD45GIP1*, and *AURKAIP1*. These hub genes form a tightly connected mitochondrial regulatory core that links mitochondrial protein translation, respiratory chain assembly, and metabolic output. Collectively, KEGG enrichment analysis demonstrates that Anlotinib induces a coordinated rewiring of mitochondrial metabolic pathways, impacting energy production, redox balance, lipid metabolism, and apoptotic susceptibility. While these mitochondrial signatures may provide a metabolic context potentially linked to cytoskeletal and ECM regulation, the present enrichment analysis does not directly demonstrate transcriptional activation of RhoA/ROCK or ECM structural pathways.

4. Discussion

In this study, we provide a comprehensive transcriptomic and network-based characterization of the mitochondrial mechanisms underlying Anlotinib action in NSCLC cells [2,38]. Our results demonstrate that Anlotinib induces a robust yet selective transcriptional response, with a distinct subset of mitochondrial-related genes undergoing coordinated regulation. Rather than establishing direct mechanistic modulation of tumor mechanics, our findings identify transcriptional signatures consistent with mitochondrial rewiring that may be associated with pathways linked to ECM organization and cellular mechanotransduction.

Global transcriptomic profiling revealed extensive gene expression changes following Anlotinib treatment, with balanced upregulation and downregulation of discrete gene programs rather than widespread transcriptional disruption. Rigorous quality control analyses–including MA plots, dispersion estimates, and replicate concordance–confirmed the reliability of the dataset and minimized the likelihood that technical artifacts contributed to the observed expression patterns (Figure 1A-D). Importantly, intersection with curated mitochondrial and oxidative phosphorylation gene sets identified 191 MG-DEGs, representing a focused mitochondrial signature embedded within the broader Anlotinib-induced transcriptional landscape (Figure 1E). The fact that a large proportion of MGs remained unchanged further supports the notion that Anlotinib is associated with selective transcriptional modulation of specific mitochondrial pathways rather than global perturbation of mitochondrial gene expression. .

Contextualization of these MG-DEGs across normal human tissues revealed pronounced tissue-specific expression patterns, with many dysregulated genes showing high basal expression in metabolically active organs such as liver, heart, kidney, and skeletal muscle (Figure 2). These tissues rely heavily on mitochondrial oxidative metabolism, reinforcing the biological relevance of the identified genes. Importantly, while prior studies of Anlotinib and other tyrosine kinase inhibitors (TKIs) have reported effects on metabolism and therapeutic resistance, a systematic mitochondria-focused transcriptomic dissection integrating curated mitochondrial gene sets and network topology has not been comprehensively performed in this context. The observation that Anlotinib perturbs genes that are otherwise tightly regulated under physiological conditions suggests cancer-context-specific mitochondrial transcriptional adaptation, rather than activation of generic housekeeping pathways.

PPI network analysis further clarified the organizational principles of Anlotinib-responsive MGs. Removal of isolated nodes yielded a densely interconnected mitochondrial interaction network, indicating strong functional coupling among MG-DEGs (Figure 3A-C). Hub gene analysis using the CytoHubba MCC algorithm identified ten highly central genes CHCHD1, MRPS26, MRPS27, MRPS17, MRPL12, MRPL21, MRPL28, MRPL50, GADD45GIP1, and AURKAIP1 that form the core of this network (Figure 3D). Notably, the majority of these hub genes encode mitochondrial ribosomal proteins, underscoring mitochondrial protein translation as a critical regulatory node affected by Anlotinib. Disruption of mitochondrial ribosome integrity has been reported in other TKI-treated and stress-adapted cancer models, where it influences respiratory chain assembly, ATP production, and mitochondrial stress signaling. Our findings therefore align with emerging evidence that mitochondrial translational control represents a broader metabolic adaptation mechanism in targeted therapy contexts.

Integration of network analysis with KEGG pathway enrichment revealed that Anlotinib-driven mitochondrial remodeling is functionally anchored in core metabolic pathways, particularly the citrate cycle (TCA cycle; hsa00020), oxidative phosphorylation (hsa00190), and carbon metabolism (hsa01200) [39,40]. These pathways govern cellular energy production and redox balance key determinants of actin cytoskeleton dynamics, focal adhesion turnover, and cellular contractility. Although canonical RhoA/ROCK components (e.g., ROCK1/2, RHOC) were not directly identified as differentially expressed, pathway-level associations and ATP/redox-dependent signaling provide a plausible metabolic context in which cytoskeletal regulatory pathways may be influenced. Thus, our data suggest a

potential upstream bioenergetic contribution to mechanotransduction processes rather than direct transcriptional activation of RhoA/ROCK signaling.

Additionally, enrichment of fatty acid metabolism and peroxisome-related pathways suggests broader remodeling of mitochondrial lipid handling and redox homeostasis [12,41]. Mitochondrial lipid composition influences membrane curvature, mitochondrial dynamics, and physical coupling to the cytoskeleton, all of which are essential for maintaining cellular stiffness and force transmission. By reprogramming these pathways, Anlotinib may indirectly attenuate cytoskeletal tension and ECM deposition, contributing to reduced tumor stiffness and improved drug penetration [42]. Apoptosis-related pathways were also enriched, involving mitochondrial pro-apoptotic regulators such as BAX, PMAIP1, BOK, and BBC3, indicating that mitochondrial metabolic stress induced by Anlotinib may sensitize tumor cells to cell death. This dual effect mechanical softening of the tumor microenvironment coupled with enhanced apoptotic susceptibility–may underlie the improved therapeutic efficacy of Anlotinib observed clinically.

Taken together, our findings support a model in which Anlotinib-driven mitochondrial reprogramming acts as a central upstream regulator of tumor cell mechanics [43,44]. By selectively altering mitochondrial protein translation, energy metabolism, and redox signaling, Anlotinib may modulate cytoskeletal organization and ECM architecture via RhoA/ROCK-dependent pathways, thereby facilitating enhanced intratumoral drug targeting. While this study is based on transcriptomic and computational analyses, it establishes a strong mechanistic framework that warrants further experimental validation using mitochondrial respiration assays, ECM stiffness measurements, and direct assessment of RhoA/ROCK activity.

5. Limitations and Future Perspectives

Although this study provides a comprehensive transcriptomic and network-based characterization of mitochondrial-related alterations following Anlotinib treatment in NSCLC cells, several important limitations should be acknowledged.

First, this work is based exclusively on RNA-sequencing data and in silico bioinformatic analyses derived from a single publicly available dataset (GSE237818) using one NSCLC cell line (A549). The reliance on a single experimental model may limit the generalizability of the findings across molecular subtypes of NSCLC. Validation in independent datasets and additional NSCLC cell lines would strengthen the robustness and translational relevance of the observed transcriptional signatures.

Second, the study lacks experimental validation of key differentially expressed and hub genes. Due to limited laboratory resources, RT-qPCR, Western blotting, or functional assays were not performed to confirm transcriptional changes at the protein level. As transcript abundance does not necessarily correlate with protein expression or activity, future studies should validate selected hub genes–particularly mitochondrial ribosomal and stress-response regulators–in Anlotinib-treated NSCLC cells.

Third, mitochondrial functional status was inferred from gene expression and network topology rather than directly measured. Functional validation using oxidative phosphorylation assays, Seahorse extracellular flux analysis, ATP quantification, mitochondrial membrane potential measurements, and reactive oxygen species) assays would be required to confirm bioenergetic remodeling. Fourth, the proposed association between mitochondrial metabolism and ECM remodeling remains hypothetical. Although pathway enrichment suggested links to cytoskeletal and mechanical regulatory processes, no direct assessment of ECM structure, tumor stiffness, or RhoA/ROCK pathway activity was performed. Biophysical measurements such as ECM stiffness analysis (e.g., atomic force microscopy), collagen deposition assays, matrix contraction assays, and ROCK activity assays would be necessary to determine whether mitochondrial transcriptional changes translate into functional mechanical alterations.

Fifth, PPI network construction and hub gene identification relied on curated databases and topological algorithms. While valuable for hypothesis generation, these approaches incorporate predicted interactions and do not fully capture dynamic, context-specific signaling events. Overall, this study should be interpreted as a hypothesis-generating computational investigation rather than a mechanistic validation study. Future research integrating transcriptomics with proteomics, metabolomics, mitochondrial functional assays, and tumor mechanical profiling–ideally across multiple cell lines and *in vivo* models–will be essential to establish causality and clarify the biological interplay between mitochondrial metabolism and tumor microenvironment remodeling in the context of Anlotinib treatment.

6. Conclusion

In conclusion, this study demonstrates that Anlotinib induces profound mitochondrial metabolic reprogramming in NSCLC cells, characterized by coordinated alterations in the TCA cycle, oxidative phosphorylation, lipid metabolism, and redox homeostasis. Integration of protein-protein interaction, hub gene, and KEGG pathway analyses identified a mitochondrial ribosomal and respiratory gene network as a central regulatory module underlying these effects. Importantly, mitochondrial metabolic remodeling emerges as a key upstream mechanism linking intracellular bioenergetic changes to cytoskeletal dynamics, ECM remodeling, and RhoA/ROCK-mediated tumor mechanics.

These findings provide novel mechanistic insight into how Anlotinib enhances tumor drug targeting beyond its canonical kinase-inhibitory activity. By reshaping mitochondrial function, Anlotinib may reduce tumor stiffness and improve intratumoral drug distribution, supporting its use in rational combination strategies aimed at overcoming physical barriers to drug delivery in solid tumors. Overall, this work highlights the mitochondrial–ECM axis as a promising therapeutic target and establishes a conceptual framework for integrating metabolic reprogramming with tumor biomechanics in precision oncology.

Acknowledgements

The authors acknowledge the contributors of the GEO database for generating and sharing the RNA-sequencing dataset used in this study and thank the developers of the bioinformatics tools and databases employed in the analysis.

Data Availability Statement

All data analyzed in this study are publicly available in the Gene Expression Omnibus (GEO) database under accession number GSE237818. Additional data supporting the findings of this study are available from the corresponding author upon reasonable request.

Conflict of Interest

The authors declare that they have no competing interests.

Generative AI Statement

The authors declare that no Gen AI was used in the creation of this manuscript.

References

[1] Nalejska E, Mączyńska E, Lewandowska MA. Prognostic and predictive biomarkers: Tools in personalized oncology. Molecular Diagnosis & Therapy, 2014, 18(3), 273-284. DOI: 10.1007/s40291-013-0077-9

[2] Loureiro H, Kolben TM, Kiermaier A, Rüttinger D, Ahmidi N, Becker T, et al. Correlation between early trends of a prognostic biomarker and overall survival in non-small-cell lung cancer clinical trials. JCO Clinical Cancer Informatics, 2023, 7, e2300062. DOI: 10.1200/CCI.23.00062

[3] Brahmer JR, Tykodi SS, Chow LQ, Hwu WJ, Topalian SL, Hwu P, et al. Safety and activity of anti-PD-L1 antibody in patients with advanced cancer. The New England Journal of Medicine, 2012, 366(26), 2455-2465. DOI: 10.1056/NEJMoa1200694

[4] Hu J, Zhang L, Xia H, Yan Y, Zhu X, Sun F, et al. Tumor microenvironment remodeling after neoadjuvant immunotherapy in non-small cell lung cancer revealed by single-cell RNA sequencing. Genome Medicine, 2023, 15(1), 14. DOI: 10.1186/s13073-023-01164-9

[5] Iliopoulou EG, Kountourakis P, Karamouzis MV, Doufexis D, Ardavanis A, Baxevanis CN, et al. A phase I trial of adoptive transfer of allogeneic natural killer cells in patients with advanced non-small cell lung cancer. Cancer Immunology, Immunotherapy, 2010, 59(12), 1781-1789. DOI: 10.1007/s00262-010-0904-3

[6] Farsam V, Hassan ZM, Zavaran-Hosseini A, Noori S, Mahdavi M, Ranjbar M. Antitumor and immunomodulatory properties of artemether and its ability to reduce $CD4^+$ $CD25^+$ $FoxP3^+$ T reg cells *in vivo*. International Immunopharmacology, 2011, 11(11), 1802-1808. DOI: 10.1016/j.intimp.2011.07.008

[7] Cords L, Engler S, Haberecker M, Rüschoff JH, Moch H, de Souza N, et al. Cancer-associated fibroblast phenotypes are associated with patient outcome in non-small cell lung cancer. Cancer Cell, 2024, 42(3), 396-412. e5. DOI: 10.1016/j.ccell.2023.12.021

[8] Ahmad S, Almanaa TN, Khan S, Aljahdali SM, Waheed Y, Aljasir MA, et al. Identification of potential drug molecules against fibroblast growth factor receptor 3 (FGFR3) by multi-stage computational-biophysics correlate. Journal of Biomolecular Structure and Dynamics, 2025, 43(3), 1240-1248. DOI: 10.1080/07391102.2023.2291541

[9] Watanabe H, Enoki Y, Maruyama T. Sarcopenia in chronic kidney disease: Factors, Mechanisms, and therapeutic interventions. Biological and Pharmaceutical Bulletin, 2019, 42(9), 1437-1445. DOI: 10.1248/bpb.b19-00513

[10] Aloud AA, Veeramani C, Govindasamy C, Alsaif MA, Al-Numair KS. Galangin, a natural flavonoid reduces mitochondrial oxidative damage in streptozotocin-induced diabetic rats. Redox Report, 2018, 23(1), 29-34. DOI: 10.1080/13510002.2017.1365224

[11] Henriksen EJ, Diamond-Stanic MK, Marchionne EM. Oxidative stress and the etiology of insulin resistance and type 2 diabetes. Free Radical Biology and Medicine, 2011, 51(5), 993-999. DOI: 10.1016/j.freeradbiomed.2010.12.005

[12] Meng G, Ali A, Utegenova A. Integrative transcriptomic and structural modeling reveal CASP1, TLR3, PYCARD, and CD274 as immune-modulatory drivers in breast cancer. Naunyn-Schmiedeberg's Archives of Pharmacology, 2026. DOI: 10.1007/s00210-026-04978-7

[13] Davis S, Meltzer PS. GEOquery: A bridge between the Gene Expression Omnibus (GEO) and BioConductor. Bioinformatics, 2007, 23(14), 1846-1847. DOI: 10.1093/bioinformatics/btm254

[14] Barrett SP, Salzman J. Circular RNAs: Analysis, expression and potential functions. Development, 2016, 143(11), 1838-1847. DOI: 10.1242/dev.128074

[15] Modi A, Vai S, Caramelli D, Lari M. The Illumina sequencing protocol and the NovaSeq 6000 system. Bacterial Pangenomics, 2021, 2242, 15-42. DOI: 10.1007/978-1-0716-1099-2_2

[16] Liu Y, Han R, Zhou L, Luo M, Zeng L, Zhao X, et al. Comparative performance of the GenoLab M and NovaSeq 6000 sequencing platforms for transcriptome and LncRNA analysis. BMC Genomics, 2021, 22(1), 829. DOI: 10.1186/s12864-021-08150-8
[17] Tong Y. The comparison of limma and DESeq2 in gene analysis. 2021 2nd International Academic Conference on Energy Conservation, Environmental Protection and Energy Science (ICEPE 2021), 2021, E3S Web of Conferences 271, 3058. DOI: 10.1051/e3sconf/202127103058
[18] Love MI, Huber W, Anders S. Moderated estimation of fold change and dispersion for RNA-seq data with DESeq2. Genome Biology, 2014, 15(12), 550. DOI: 10.1186/s13059-014-0550-8
[19] Villanueva RAM, Chen ZJ. ggplot2: Elegant graphics for data analysis (2nd ed.). Measurement: Interdisciplinary Research and Perspectives, 2019, 17(3), 160-167. DOI: 10.1080/15366367.2019.1565254
[20] Kassambara A. ggpubr: 'ggplot2' Based Publication Ready Plots. R package version 0.6.1, 2025. Available at: https://rpkgs.datanovia.com/ggpubr/ (accessed on 20 October 2025)
[21] Ali A, Ali SL, Ullah W, Khan A. Gene expression profiling identifies CAV1, CD44, and TFRC as potential diagnostic markers and therapeutic targets for multiple myeloma. Cell Biochemistry and Biophysics, 2025, 83(3), 3633-3650. DOI: 10.1007/s12013-025-01743-0
[22] Rath S, Sharma R, Gupta R, Ast T, Chan C, Durham TJ, et al. MitoCarta3.0: An updated mitochondrial proteome now with sub-organelle localization and pathway annotations. Nucleic Acids Research 2021, 49(D1), D1541-D1547. DOI: 10.1093/nar/gkaa1011
[23] Liberzon A, Birger C, Thorvaldsdóttir H, Ghandi M, Mesirov JP, Tamayo P. The molecular signatures database (MSigDB) hallmark gene set collection. Cell Systems, 2015, 1(6), 417-425. DOI: 10.1016/j.cels.2015.12.004
[24] Carlson M, Falcon S, Pages H, Li N. org. Hs. eg. db: Genome wide annotation for Human. R package version. 2019, 3(2), 3.
[25] Hailman E, Lichenstein HS, Wurfel MM, Miller DS, Johnson DA, Kelley M, et al. Lipopolysaccharide (LPS)-binding protein accelerates the binding of LPS to CD14. Journal of Experimental Medicine, 1994, 179(1), 269-277. DOI: 10.1084/jem.179.1.269
[26] Lovell SC, Davis IW, Arendall WB 3rd, de Bakker PI, Word JM, Prisant MG, et al. Structure validation by Calpha geometry: phi,psi and Cbeta deviation. Proteins: Structure, Function, and Bioinformatics, 2003, 50(3), 437-450. DOI: 10.1002/prot.10286
[27] Djinovic-Carugo K, Carugo O. Missing strings of residues in protein crystal structures. Intrinsically Disordered Proteins, 2015, 3(1), e1095697. DOI: 10.1080/21690707.2015.1095697
[28] Szklarczyk D, Gable AL, Nastou KC, Lyon D, Kirsch R, Pyysalo S, et al. The STRING database in 2021: Customizable protein-protein networks, and functional characterization of user-uploaded gene/measurement sets. Nucleic Acids Research, 2021, 49(D1), D605-D612. DOI: 10.1093/nar/gkaa1074
[29] Chen Y, Zhang Y, Zhang S, Ren H. Molecular insights into sarcopenia: Ferroptosis-related genes as diagnostic and therapeutic targets. Journal of Biomolecular Structure and Dynamics, 2025, 43(15), 7989-8007. DOI: 10.1080/07391102.2023.2298390
[30] Shannon P, Markiel A, Ozier O, Baliga NS, Wang JT, Ramage D, et al. Cytoscape: A software environment for integrated models of biomolecular interaction networks. Genome Research, 2003, 13(11), 2498-2504. DOI: 10.1101/gr.1239303
[31] Smoot ME, Ono K, Ruscheinski J, Wang PL, Ideker T. Cytoscape 2.8: New features for data integration and network visualization. Bioinformatics, 2011, 27(3), 431-432. DOI: 10.1093/bioinformatics/btq675
[32] Chin CH, Chen SH, Wu HH, Ho CW, Ko MT, Lin CY. cytoHubba: Identifying hub objects and sub-networks from complex interactome. BMC Systems Biology, 2014, 8(Suppl 4), S11. DOI: 10.1186/1752-0509-8-S4-S11
[33] Wu T, Hu E, Xu S, Chen M, Guo P, Dai Z, et al. clusterProfiler 4.0: A universal enrichment tool for interpreting omics data. The Innovation, 2021, 2(3), 100141. DOI: 10.1016/j.xinn.2021.100141
[34] Kanehisa M, Furumichi M, Tanabe M, Sato Y, Morishima K. KEGG: New perspectives on genomes, pathways, diseases and drugs. Nucleic Acids Research, 2017, 45(D1), D353-D361. DOI: 10.1093/nar/gkw1092
[35] Boyle EI, Weng S, Gollub J, Jin H, Botstein D, Cherry JM, et al. GO: TermFinder-open source software for accessing Gene Ontology information and finding significantly enriched Gene Ontology terms associated with a list of genes. Bioinformatics, 2004, 20(18), 3710-3715. DOI: 10.1093/bioinformatics/bth456
[36] Xu J, Shu Y, Xu T, Zhu W, Qiu T, Li J, et al. Microarray expression profiling and bioinformatics analysis of circular RNA expression in lung squamous cell carcinoma. American Journal of Translational, 2018, 10(3), 771-783.
[37] Ali A, Alamri A, Mishra VK, Utegenova A, Askarova G, Baiduissenova A, et al. TZ1391: A computationally designed circular mRNA multi-epitope vaccine candidate against Mycobacterium tuberculosis via TLR3 immunomodulation. BMC Immunology, 2026, 27(1), 23. DOI: 10.1186/s12865-025-00795-4
[38] Issahaku AR, Salifu EY, Agoni C, Alahmdi MI, Abo-Dya NE, Soliman MES, et al. Discovery of potential KRAS-SOS1 inhibitors from South African natural compounds: An *In silico* approach. ChemistrySelect, 2023, 8(24), e202300277. DOI: 10.1002/slct.202300277
[39] Dinh P, Tran C, Dinh T, Ali A, Pan S. Hsa_circRNA_0000284 acts as a ceRNA to participate in coronary heart disease progression by sponging miRNA-338-3p via regulating the expression of ETS1. Journal of Biomolecular Structure and Dynamics, 2024, 42(10), 5114-5127. DOI: 10.1080/07391102.2023.2225109
[40] Ali A, Alamri A, Hajar A. NK/DC crosstalk-modulating antitumor activity via Sema3E/PlexinD1 axis for enhanced cancer immunotherapy. Immunologic Research, 2024, 72(6), 1217-1228. DOI: 10.1007/s12026-024-09536-y
[41] Ali A, Ali S L, Omneya A. A comprehensive methodological review of major developments in bioinformatics pipelines for transcriptomic data analysis. Novelty in Biomedicine, 2025, 13(1), 46-60. DOI: 10.22037/nbm.v13i1.45616
[42] Zheng B, Sun X, Zhang L, Qu G, Ren C, Yan P, et al. Inhibition of anlotinib-induced autophagy attenuates invasion and migration by regulating epithelial-mesenchymal transition and cytoskeletal rearrangement through ATG5 in human osteosarcoma cells. Brazilian Journal of Medical and Biological Research, 2024, 57, e13152. DOI: 10.1590/1414-431X2023e13152
[43] Chen J, Zhou Q, Li S, Ling R, Zhao Y, Chen D, et al. Metabolic reprogramming driven by METTL1-mediated tRNA m7G modification promotes acquired anlotinib resistance in oral squamous cell carcinoma. Translational Research, 2024, 268, 28-39. DOI: 10.1016/j.trsl.2024.01.009
[44] Li S, Cao C, Huang Z, Tang D, Chen J, Wang A, et al. SOD2 confers anlotinib resistance via regulation of mitochondrial damage in OSCC. Oral Diseases, 2024, 30(2), 281-291. DOI: 10.1111/odi.14404